The Astrophysical Journal, 575:493–505, 2002 August 10

THE IMPACT OF SOLAR-LIKE VARIABILITY ON THE DETECTABILITY OF TRANSITING TERRESTRIAL PLANETS

Jon M. Jenkins
SETI Institute/NASA Ames Research Center, MS 245-3, Moffett Field, CA 94035; jjenkins@mail.arc.nasa.gov
Received 2001 November 19; accepted 2002 April 10

ABSTRACT

Transit photometry is a promising method for discovering extrasolar planets as small as Earth from space-based photometers, and several near-term photometric missions are on the drawing board. In particular, NASA's recently selected *Kepler* mission is devoted primarily to detecting extrasolar planets. The success of these efforts depends in part on the ability to detect transit signatures against the inherent photometric variability of the target stars. While other noise sources such as shot noise and CCD noise are under the control of the instrument designers, this one is not. The photometric variability of solar-like stars presents a fundamental lower limit to the minimum detectable planet radius for a given star and number of observed transits. In this paper we examine the capability of such missions using bolometric data for the only star for which sufficient photometric precision exists to address this question: the Sun. The results indicate that solar-like variability does not prevent the detection of Earth-sized planets even for stars rotating significantly faster than the Sun. Four transits are detectable for $m_v = 12$ stars with rotation periods as short as $\sim$21 days, while six transits allow detection for stellar rotation periods as short as $\sim$16 days. Indeed, the limits posed by solar-like variability allow for the detection of planets significantly smaller than Earth orbiting Sun-like stars. Planets as small as 0.6 Earth radii exhibiting at least six transits can be detected orbiting bright ($m_v = 10$) solar analogs.

Subject headings: methods: data analysis — planetary systems — techniques: photometric

1. INTRODUCTION

The search for extrasolar planets has produced $\sim$100 discoveries by the radial velocity method over the past 6 yr. All of these planets are similar in size and mass to Jupiter, and the lower limit of such searches is in the neighborhood of Saturn's mass. The orbits of these gas giant planets surprised most planetary astronomers and theorists, as they are not circular for the most part, but are significantly eccentric, certainly much more so than the dispersion of the eccentricity of the planets in our solar system would indicate. These discoveries have fueled the desire to detect much smaller planets, and missions to detect planets as small as Earth have been proposed to NASA and to ESA. These include NASA's recently selected *Kepler* mission and ESA's proposed *Eddington* mission. Beyond detecting planets, NASA's Terrestrial Planet Finder (TPF) mission is envisioned as an infrared-nulling interferometer with the ambitious goal of imaging Earth-sized planets orbiting nearby stars. The distance to which TPF must search and, hence, its physical scale are dictated by the frequency of Earth-sized planets about solar-like stars in our Galactic neighborhood. The only technology identified that appears capable of delivering this crucial information is transit photometry. While gravitational microlensing might also play a role in accumulating statistical information about planets significantly smaller than Jupiter, it does so only for stars too distant for the planned scope of TPF.

In transit photometry, nearly continuous flux measurements of many individual stars are used to search for signatures caused by the transit of a planet crossing a stellar disk. The amplitude of the flux reduction reveals the size ratio of the planet to the star, while the time interval between transits gives the orbital period. From Kepler's third law and from knowledge of the stellar mass and size, the planetary size and semimajor axis can be determined (Borucki & Summers 1984; Schneider & Chevreton 1990). Recently, transit photometry confirmed the planetary nature of HD 209458b first by ground-based photometry (Charbonneau et al. 2000; Henry et al. 2000) and subsequently by space-based photometry (Castellano et al. 2000; Robichon & Arenou 2000; Brown et al. 2001). Transit photometry searches are not new. Since 1994, the Transits of Extrasolar Planets (TEP) Network (Deeg et al. 1998; Doyle et al. 2000; Jenkins, Doyle, & Deeg 2000) has been observing one of the smallest known eclipsing binary systems, CM Draconis, for evidence of small transiting planets and large nontransiting ones. Several groups are attempting to detect 51 Peg–type planets from the ground (see, e.g., Borucki et al. 2001; Brown & Charbonneau 2000; Henry et al. 2000; Everett et al. 2000), while others are using spaceborne instruments, including the *Hubble Space Telescope* (*HST*) (Gilliland et al. 2000; Brown et al. 2001) and the *Hipparcos* data archive (Laughlin 2000).

In order to detect terrestrial-sized planets, unprecedented photometric precision is required. The radius of the Earth is approximately 1/100 that of the Sun. Consequently, a transit of the Sun by the Earth blocks $\approx 1 \times 10^{-4}$ of the flux from the solar disk. Traditional ground-based photometry appears to be limited to a precision of $\sim 1 \times 10^{-3}$ to 1×10^{-4} for 1–4 m class telescopes (see e.g., Henry 1999; Olsen 1977; Frandsen, Dreyer, & Kjeldsen 1989; Gilliland & Brown 1992; Young et al. 1991; Dravins et al. 1998). The attainable precision of ground-based CCD photometers is not limited by shot noise or instrumental noise, however. Noise induced by the intervening terrestrial atmosphere is the chief culprit, injecting scintillation noise and transparency variations into the measurements. Scattering and dispersion in the Earth's atmosphere result in color-dependent extinction effects. In addition, there are clouds and overflights of satellites and planes through the desired field of view. Moreover, the timescales for ground-based observa-

tions present a problem as well, conflicting with the timescales pertinent to transits of inner planets (2–16 hr). There are only a limited number of photometric hours available each night (8–12) and a limited number of photometric nights available each observing season (see, e.g., Borucki et al. 2001). Clearly, space-based photometry offers many advantages over ground-based photometry from the perspective of providing uninterrupted measurements of uniform quality. With respect to instrumental precision, laboratory measurements have clearly demonstrated that differential CCD photometers can easily achieve this requisite precision (Robinson et al. 1995; Jenkins et al. 1997, 2000b; Koch et al. 2000). Indeed, observations of transits of 209458b with *HST*'s Space Telescope Imaging Spectrograph (STIS) instrument produced an absolute photometric data set with sufficient precision to have detected an Earth-sized moon orbiting the inflated Jovian planet in that system if one were present (Brown et al. 2001). In contrast to ground-based photometric searches for Jupiter-sized planets, stellar variability is likely to be a chief noise source for space-based, photometric missions searching for Earth-sized planets.

The impact of solar-like variability on the detectability of transiting planets has been studied previously. Perhaps the first paper is Borucki et al. (1985), which examined the question in light of measurements by the Active Cavity for Irradiance Monitoring (ACRIM) on board the *Solar Maximum Mission* (*SMM*). This is one of the few papers to recognize the problems posed by the red-noise nature of solar variability. Moreover, the statistical nature of the solar variations is not stationary. During solar maximum, the Sun is much more magnetically active than at solar minimum, producing many more Sun spots and plages and their associated photometric features. At solar maximum, for example, the fractional sample standard deviation of solar irradiance is $\sim 4 \times 10^{-4}$, while at solar minimum, when few if any spots are present, it is $\sim 1 \times 10^{-4}$. As will become evident, the timescale of variability is an important factor in determining the detectability of planetary transits.

ACRIM's measurements, however, were complicated by the presence of significant instrumental noise and severe sampling problems resulting from the spacecraft's low Earth orbit. The results should be viewed as highly conservative regarding the detectability of Earth-sized transits in the presence of solar-like variability. Recently, Deeg, Favata, & the *Eddington* Science Team (1998) and Bordé, Rouan, & Léger (2001) predicted the performance of the *Eddington* and *COROT* missions, respectively. Both papers assume that the observational noise can be filtered to yield white-noise time series, which can then be subjected to transit searches. Hence, both papers assume a given effective white-noise variance due to solar variability in the subsequent calculations. Unfortunately, the effective white-noise variance posed by a red-noise source is a function of both the desired signal and the accompanying white-noise sources. For signal detection purposes, the effective white noise cannot be represented as a unique value that can then be added in quadrature with other white-noise sources. Thus, without a comprehensive analysis, misleading expectations for the signal-to-noise ratio (S/N) of transit events might result. A paper that does take the nonwhite nature of solar-like variations into account is that of Defay, Deleuil, & Barge (2001). They approach the problem for Centre National d'Études Spatiale's planned *COROT* mission using segments of data from *SOHO* observations and a Bayesian detector that detects periodic signals of any shape. Such a detector is suboptimal from the standpoint of detecting transits, however, which are highly constrained to timescales of a few hours to roughly 16 hr for terrestrial planets.

In contrast to previous efforts, we examine 5.2 yr of DIARAD/*SOHO* measurements to study the effects of solar-like variability on the detectability of transiting planets, presenting the most complete and comprehensive treatment of the problem to date. We describe in detail for the first time a realizable, nearly optimal, adaptive detector capable of dealing with the time-varying nature of the expected nonwhite noise from stellar variations. In addition, we assess the detection threshold required to control the total number of false alarms without any assumptions about the statistics of the underlying observational noise.

The paper is organized as follows: We present the DIARAD/*SOHO* measurements of solar variability in § 2. The problem of detecting signals in noise is briefly reviewed in § 3, leading to a wavelet-based, adaptive matched filter detector. This section is technically complete, presenting all the detailed mathematics necessary to implement the proposed detector. In § 4 this detector is applied to the DIARAD time series to study the impact of solar variability under a variety of scenarios. Noise representing instrumental and shot-noise sources for *Kepler* are added to the DIARAD time series to determine the detectability of Earth-sized transits as a function of transit duration and stellar brightness throughout the solar cycle. We next examine the detectability of transits as a function of stellar rotation by scaling and resampling the DIARAD time series to simulate stars rotating faster and slower than the Sun. This is followed by the results of a bootstrap analysis in § 5 to assess the appropriateness of using Gaussian statistics to predict the performance of transit photometry campaigns. We conclude in § 6 by summarizing the results and giving suggestions for future work. The bootstrap algorithm for assessing the distribution of the null statistics is presented in the Appendix.

2. The DIARAD/*SOHO* OBSERVATIONS

In order to study the capabilities of missions such as *Kepler* and *Eddington*, we take measurements from the DIARAD instrument on board the *SOHO* spacecraft as a proxy for all solar-like stars. DIARAD is a redundant, active-cavity radiometer on board *SOHO* that measures the white-light irradiance from the Sun every 3 minutes (Fröhlich et al. 1997). The second cavity is normally kept closed and is opened occasionally to calibrate the primary cavity, which ages throughout the mission with exposure to the Sun. The instrumental noise for a single 3 minute measurement is 0.1 W m^{-2} (Steven Dewitte 1999, personal communication). The DIARAD measurements considered here consist of 5.2 yr of data that begin near solar minimum in 1996 January and extend to 2001 March, just past solar maximum.

The data are not pristine: there are gaps in the data set, the largest of which lasts 104 days, and there are obvious outliers in the data. In particular, a set of 10 or 11 consecutive, anomalous points appears almost every 60 days. Each set begins with a point several W m^{-2} below the trend line, with the remaining 9 or 10 points lying approximately 6 W m^{-2} above the trend line. Nevertheless, the DIARAD time series is the most uniformly sampled, lowest noise data set available. We have taken the liberty of removing the

obvious outliers, such as the ones occurring every 60 days, and a small number of isolated outliers that appear to occur randomly. We have not removed some of the data segments that appear to be corrupted in more subtle ways. An example of these is given by data on the edges of gaps in the data set, which often have atypically large slopes. Fully 83% of the data samples are available (62% of the missing points are represented by the three largest data gaps). For our purposes, a contiguous, completely sampled data set is highly desirable. This is mainly for computational convenience (to avoid division by zero errors), and the filled-in points are largely neglected in addressing the detectability of transits against stellar variability. To that end, the missing points have been filled in by reflecting a segment on either side of each gap across the gap. We combine the two segments by taking the sum of each multiplied by a linear taper directly proportional to the distance from the closest edge of the gap. This procedure naturally preserves continuity of the data, and it preserves the correlation structure to a large degree. Some smoothing of the small-scale structure occurs, however, as the procedure takes the average of two segments of a noise process. We have adjusted the filled-in data to reduce the amount of smoothing using a technique described in § 4.

Figure 1 shows the DIARAD time series, binned to 1 hr. Filled-in gaps of at least a day in duration are denoted by the horizontal line segments at 1365.5 W m^{-2}. The average solar flux during the 5.2 yr of observation is 1366.6 W m^{-2}. Note that on this scale, an Earth-sized transit (84 parts per million [ppm]) is 0.115 W m^{-2}. The sample standard deviation of the data set is 0.5 W m^{-2}. This would seem to imply that detecting Earth-sized transiting planets might be a terribly difficult, if not impossible, task. The solar variability is not a white-noise process, however, and most of the noise power occurs on very long timescales compared to the duration of a central transit of planets with orbital periods up to 2 yr about a solar-like star (2–16 hr). This is made clear by Figure 2, which exhibits the power of the DIARAD time series as a function of timescale near solar minimum (1996) and near solar maximum (2000) along with the energy at

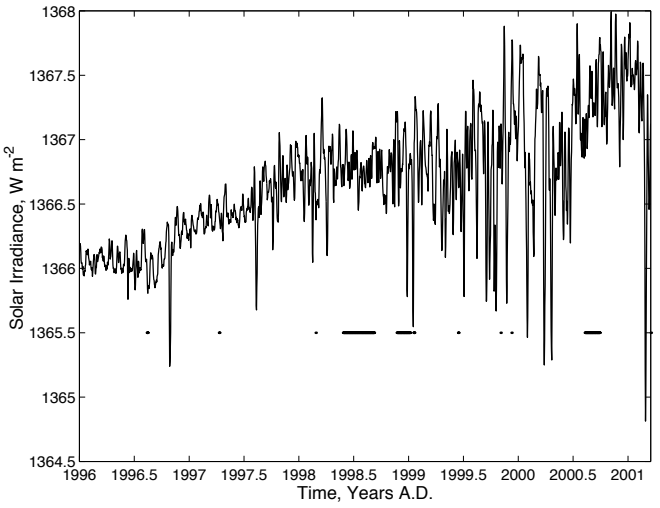

FIG. 1.—Time series of solar irradiance as measured by the DIARAD instrument on board *SOHO* from 1996 January 1 through 2001 March binned to 1 hr. Gaps of a day or longer are denoted by the horizontal segments at 1365.5 W m^{-2}.

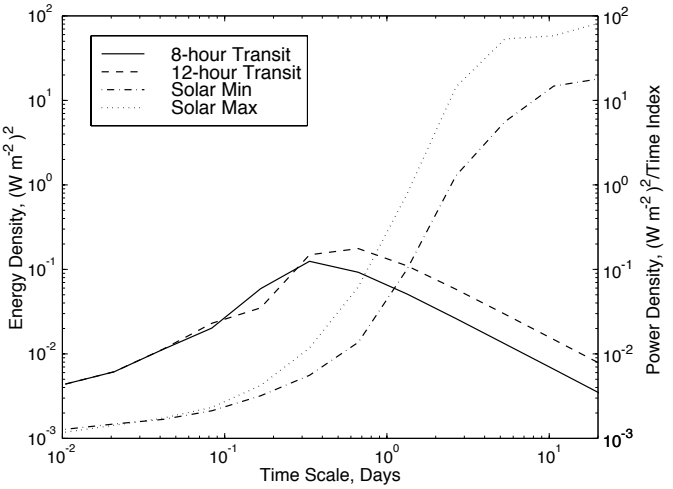

FIG. 2.—Distribution of power as a function of timescale from a wavelet analysis of the time series of solar irradiance as measured by the DIARAD instrument on board *SOHO* for the years of 1996, near solar minimum (*dash-dotted curve*), and 2000, near solar maximum (*dotted curve*). The timescale labeling is approximate, as no unique definition for it exists. The distribution of energy with timescale is also plotted for an Earth-sized, 8 hr transit (*solid curve*) and for a 12 hr transit (*dashed curve*). The area under the transit curves and above the solar variability curves indicates that the transits are readily detectable against the solar variations.

each timescale for Earth-sized, 8 and 12 hr transits. These curves were obtained by a wavelet analysis described in § 3. Note that at timescales shorter than 1 day, the ratio of the transit energy to the power of the solar time series is much greater than 1. This indicates that transits of Earth-sized planets are highly detectable against solar-like variability, with low intrinsic noise, space-based observations.

3. DETECTION THEORY

Suppose we wish to detect a signal $s(n)$ (with time sample index n) in observational data $x(n)$. Further, suppose that $x(n)$ is composed solely of Gaussian noise $w(n)$ [i.e., $x(n) = w(n)$] or that $x(n)$ is the sum of the signal plus noise [i.e., $x(n) = w(n) + s(n)$]. Time series will usually be denoted by the functional form used here; however, it is sometimes convenient to use vector notation: $\boldsymbol{x} = x(n),\ n = 1, \ldots, N$, where N is the length of the time series. Under these conditions, the optimal detector is a matched filter of the form

$$l = \frac{\boldsymbol{x}^T R^{-1} \boldsymbol{s}}{\sqrt{\boldsymbol{s}^T R^{-1} \boldsymbol{s}}} = \frac{(R^{-1/2}\boldsymbol{x})^T (R^{-1/2} s)}{\sqrt{(R^{-1/2}\boldsymbol{s})^T (R^{-1/2} s)}}\,, \qquad (1)$$

where R is the autocorrelation matrix of the noise, $w(n)$, and T is the transpose operator (see, e.g., Kay 1999). The value of the detection statistic, l, determines whether a detection has been made by comparing it to a given threshold, η. This threshold is chosen so that the probability of a false detection occurring is small by some objective criterion. In the case of *Kepler*, the threshold is set so that no more than one false alarm is expected for the entire mission, which consists of searching light curves of more than 100,000 stars for transiting planets with orbital periods up to 2 yr. As there are $\approx 2 \times 10^7$ independent tests per star, there are a total of 2×10^{12} tests yielding a threshold of 7.1 σ, assuming Gaussian statistics (Jenkins, Caldwell, & Borucki 2002).

The detection statistic l has the following properties. If no signal is present, l is a random variable drawn from a zero-mean, unit-variance, white Gaussian noise (WGN) process. On the other hand, if the signal $\boldsymbol{s}$ is present, l again has unit variance, but it has a mean equal to $(\boldsymbol{s}^T R^{-1}\boldsymbol{s})^{1/2}$. To interpret this quantity, note that for white noise, R is diagonal with $R = \sigma^2 I$, where σ^2 is the variance of the noise and I is the identity matrix. Hence, the detectability of a signal is determined by the ratio of the energy of the whitened signal to the power of the whitened noise (the energy per unit time). For a given detection threshold, η, the detection rate, P_D, and the false-alarm rate, $P_{\rm FA}$, can be determined from

$$P_D = \frac{1}{\sqrt{2\pi}} \int_{\eta - \langle l \rangle}^{\infty} \exp\left(-\frac{y^2}{2}\right) dy \,, \tag{2}$$

$$P_{\rm FA} = \frac{1}{\sqrt{2\pi}} \int_{\eta}^{\infty} \exp\left(-\frac{y^2}{2}\right) dy \,, \tag{3}$$

respectively, where $\langle l \rangle$ is the mean detection statistic or S/N of the signal $\boldsymbol{s}$. Note that for transit photometry, three or more transits are usually required to detect a planet, as the confidence in the detection is provided by the exquisite repeatability of the events, and too, the single-transit S/N may not be sufficient to conclude that a detection has occurred. Thus it is the total S/N of a set of three or more transits that determines the detection rate. Equations (2) and (3) allow the performance of a photometric campaign to be readily established, assuming that the effective number of independent tests to be conducted per star is known, together with the total number of stars and the mean S/N of a set of transit events.

Equation (1) can be rewritten as the dot product of the whitened data vector $\tilde{\boldsymbol{x}} = R^{-1/2}\boldsymbol{x}$ with the whitened signal vector $\tilde{\boldsymbol{s}} = R^{-1/2}\boldsymbol{s}$ normalized by the magnitude of $\tilde{\boldsymbol{s}}$: $l = \tilde{\boldsymbol{x}} \cdot \tilde{\boldsymbol{s}}/|\tilde{\boldsymbol{s}}|$. From the second equality in equation (1), we see that the optimal detector consists of the cascade of a whitening filter with a matched filter (also called a correlation receiver). The difficulty lies in designing the whitening filter itself, as the correlation matrix R is often unavailable. The design of an appropriate whitening filter is the subject of the remainder of this section.

If the mean value and the correlation structure of the noise process are stationary (i.e., constant in time) and certain additional mild conditions are met, equation (1) can be expressed in the frequency domain as per Kay (1999):

$$l = \int_{-\pi}^{\pi} \frac{X(\omega)S^*(\omega)d\omega}{P(\omega)} \Bigg/ \sqrt{\int_{-\pi}^{\pi} \frac{S(\omega)S^*(\omega)d\omega}{P(\omega)}}, \tag{4}$$

where $X(\omega)$ and $S(\omega)$ are the Fourier transforms of the data and signal, respectively, asterisks denote complex conjugation, and $P(\omega)$ is the power spectrum of the noise. Kay (1999) suggested an adaptive matched filter based on equation (4) using a smoothed periodogram to estimate $P(\omega)$. This approach is fine for noise processes that are weakly colored or white, but not for $1/f$-type processes such as solar variability. Simply smoothing the periodogram with a moving average filter tends to reduce the apparent spectral slope of these processes significantly, yielding an inaccurate power spectrum estimate. Alternatively, Kay's method may be modified by using multitaper spectrum approaches to estimate the noise power spectrum, minimizing the "leakage" of the effective data window. Several choices for tapers are available, including sinusoidal families (Riedel & Sidorenko 1995), which approximate optimal tapers minimizing the asymptotic bias of the estimate. Alternatively, prolate spheroidal sequences are widely acknowledged to yield optimal spectrum estimates minimizing the spectral leakage outside a given resolution bandwidth and have been used with great success to examine p-mode oscillations in the solar power spectrum (see, e.g., Walden, Percival, & McCoy 1998). While good results can be obtained using a modification of Kay's approach, there are computational issues to consider. The length of the window used to estimate the periodogram must be chosen in some way, as well as the number of adjacent data segments to be used to provide additional smoothing of the power spectrum estimate. Moreover, the sensitivity of the detector to a transit-like signal depends on the location of the transit pulse within the window. It would seem that for the best results, a periodogram centered at each possible transit location needs to be computed, further increasing the computational burden. We propose a wavelet-based approach using an overcomplete wavelet transform (OWT) of the data and the signal to be detected. The wavelet domain is a natural one for designing time-varying filters since it *is* a joint time-frequency representation of a waveform. In addition, the overcomplete wavelet expansion admits a filter-bank implementation with a direct interpretation in terms of equation (4). As such, the properties of Kay's adaptive detector should hold for the detector described here; namely, that the detector would be asymptotically efficient (ideal) if an independent realization of the noise process were available.

First, let us review wavelets briefly. A wavelet transform is similar to the Fourier transform in that the wavelet coefficients are the projection of the original data vector onto a set of basis functions. In the case of wavelets, however, the basis functions are concentrated in time as well as in frequency. Moreover, unlike the Fourier basis, there is an infinity of possible choices for wavelet bases that trade off resolution in frequency for resolution in time. (This also implies that there is not a unique definition of the term "timescale" for wavelet transforms as there is for "frequency" for the Fourier transform.) The first orthogonal nontrivial wavelets were obtained by Debauchies (1988), who was interested in obtaining a continuous wavelet transform through iterations of a discrete time algorithm. Somewhat earlier, however, Smith & Barnwell (1984) succeeded in designing critically sampled, perfect-reconstruction, octave-band filter banks. Debauchies' wavelets are special cases of those filters meeting the conditions specified by Smith and Barnwell, such that the limiting process is a continuous time wavelet transform. The methodology we adopt is based on a filter-bank implementation of an overcomplete discrete-time wavelet transform. Hence, we will approach the subject from the viewpoint of filter banks as per Vetterli & Kovačević (1998).

Figure 3 shows a dyadic, critically sampled filter bank. In the first stage in the process, the time series $x(n)$ is separated into two channels by filters with responses $H_L(\omega)$ and $H_H(\omega)$. Each filtered signal component is then downsampled by a factor of 2 (essentially, every other sample is discarded). The high-pass signal, $x_1(n)$, is not subjected to further filtering in the analysis section. The low-pass signal, however, is treated in an identical manner as its predecessor, $x(n)$, and the process is iterated $M - 1$ times, for a total of M output channels. For our purposes, all we need to know

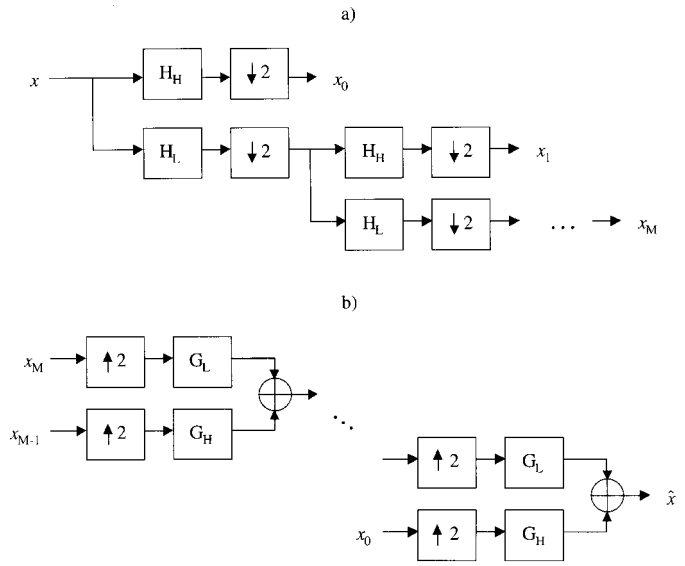

FIG. 3.—Block diagram of a filter-bank implementation of a critically sampled, discrete-time wavelet expansion of a time series; (*a*) shows the analysis section, which partitions a time series into different channels with complementary passbands, and (*b*) illustrates the synthesis section that reconstructs the original time series from the set of channels.

is that $H_L(\omega)$ is a low-pass filter and that $H_H(\omega)$ is a high-pass filter, and that these filters isolate complementary frequency components of the time series $x(n)$. Corresponding to $H_L(\omega)$ and $H_H(\omega)$ are reconstruction filters $G_L(\omega)$ and $G_H(\omega)$ such that the signal $x(n)$ is exactly equal to its reconstruction $\hat{x}(n)$. The equivalent filter for each channel in Figure 3 can be determined explicitly, and we will refer to these filters from the highest center frequency to the lowest as $\{h_1(n), h_2(n), \ldots, h_M(n)\}$. The output signals corresponding to these filters will be designated $\{x_1(n), x_2(n), \ldots, x_M(n)\}$, respectively.

Figure 4 shows the frequency response of each filter in a filter-bank implementation of a discrete-time wavelet expansion of a time series out to $M = 16$. Figure 4*a* shows the frequency axis on a linear scale, while Figure 4*b* is plotted with a log scale for the frequency axis. The filters enjoy a "constant-Q" property. That is, the quality factor (Q) defined to be the ratio of the center frequency of a bandpass filter to its FWHM, is constant for all but the final filter. In the following analysis, we omit the decimation operators ("$\downarrow 2$") in Figure 3*a* and replace each filter following a decimation operator with the result of up-sampling it by 2 (i.e., we retain the same effective filters as those of the critically sampled filter bank). This leads to an overcomplete wavelet expansion of a filtered time series. The price we pay is that the representation is highly redundant, increasing the computational burden, since we must now filter the samples discarded in the critically sampled implementation. The gain achieved is the shift invariance of the OWT of a time series. Therefore, the OWT of the convolution of two time series is the same as convolving the OWT coefficients of one time series at each scale with the corresponding coefficients of the other time series. This is not the case for the critically sampled wavelet transform. To make this explicit, let

$$\mathbb{W}\{x(n)\} = \{x_1(n), x_2(n), \ldots, x_M(n)\} \tag{5}$$

be the overcomplete wavelet transform of $x(n)$, where

$$x_i(n) = h_i(n) * x(n), \quad i = 1, 2, \ldots, M \tag{6}$$

and the asterisk denotes convolution. Then we have

$$\mathbb{W}\{x(n) * y(n)\} = \{x_1(n) * y_1(n), x_2(n) * y_2(n), \ldots, x_M(n) * y_M(n)\}\,. \tag{7}$$

A remark is in order regarding the implementation of the decimated, discrete time-wavelet transform. Normally, in order to ensure that the number of output points equals the number of input points, the convolutions performed on the data set are circular. In other words, the signal vector is treated as if it were periodic with period N, the length of the data set. If N is a power of 2, then the convolutions can be performed efficiently with fast Fourier transforms. We adopt this convention as well, applying it to the overcom-

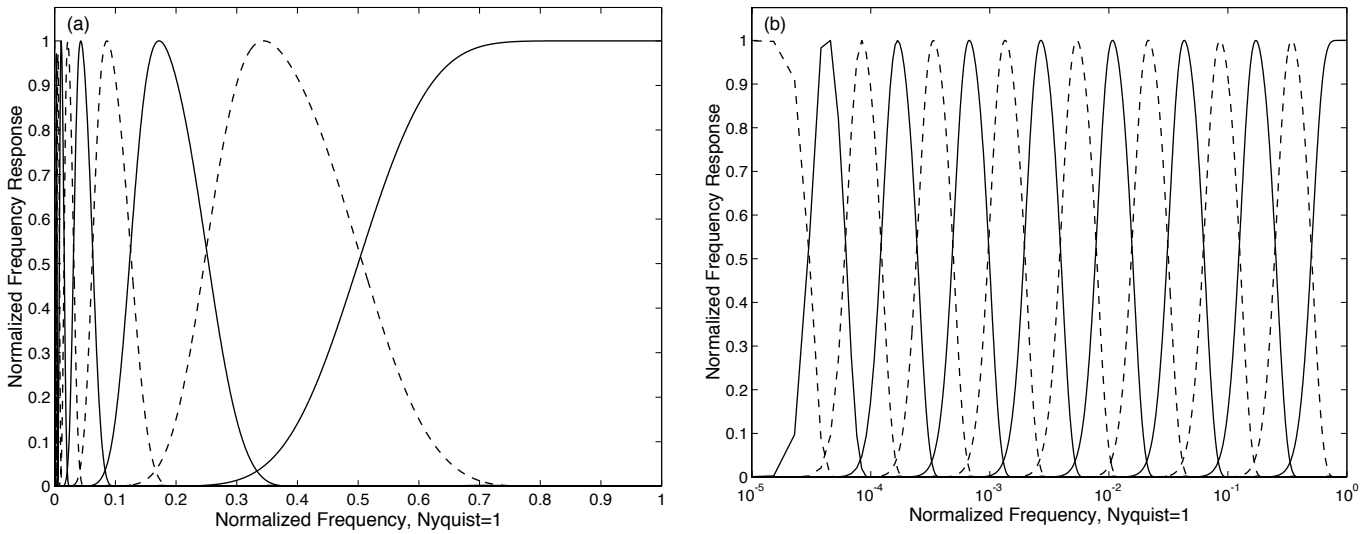

FIG. 4.—Frequency response of the filters in a filter-bank implementation of a discrete time-wavelet expansion of a time series using Debauchies' 12 tap filter; (*a*) shows the frequency responses on a linear frequency scale, and (*b*) has a logarithmic frequency scale, illustrating the "constant-Q" property of an octave-band wavelet analysis.

plete discrete-time wavelet transform such that each $x_i(n), i = 1, \ldots, M$ is an N-point sequence. Moreover, we will not distinguish between circular and noncircular convolution unless there is a reason to do so (i.e., a relationship holds for one but not the other).

One additional property is required before we can obtain a wavelet-based expression for a matched filter. We need to be able to express the dot product between two vectors in the wavelet domain. For an overcomplete, dyadic wavelet expansion, the following relationship holds:

$$\boldsymbol{x} \cdot \boldsymbol{y} = \sum_{i=1}^{M} 2^{-\min(i,M-1)} \boldsymbol{x}_i \cdot \boldsymbol{y}_i \,, \tag{8}$$

where $\boldsymbol{x}$ and $\boldsymbol{y}$ are data vectors (time series). The restriction of the power of 2 in equation (8) is necessary because the last two channels of the OWT have the same bandwidth. Equation (8) can be established from Parseval's relation for tight frames (Vetterli & Kovačević 1998). This result, in turn, should agree with our intuition, as each time we iterate the dyadic filter bank of Figure 3, we double the number of samples representing the low-pass channel output from the previous iteration.

We are now in the position to recast equation (4) in terms of the overcomplete wavelet expansion. The whitening filter is implemented by simply scaling each channel of the filter bank by a time-varying value inversely proportional to the local standard deviation of the data in that channel. The bandwidth in the channel helps determine the time frame over which the standard deviation is estimated. If the window is K points long for the smallest scale, then it should be $2^{i-1}K$ for the ith channel. The window should also be much longer than the transit duration of interest so that it will not itself be perturbed by a transit, thereby reducing the detectability of transits. On the other hand, the window should be kept short enough to track changes in the statistics of the underlying observational noise. Empirically we find that a window length 10 times the duration of a transit works well. The detection statistic, then, is computed by multiplying the whitened wavelet coefficients of the data by the whitened wavelet coefficients of the transit pulse and then applying equation (8):

$$\begin{aligned} l &= \frac{\tilde{\boldsymbol{x}} \cdot \tilde{\boldsymbol{s}}}{\sqrt{\tilde{\boldsymbol{s}} \cdot \tilde{\boldsymbol{s}}}} \\ &= \frac{\sum_{i=1}^{M} 2^{-\min(i,M-1)} \sum_{n=1}^{N} [x_i(n)/\hat{\sigma}_i(n)][s_i(n)/\hat{\sigma}_i(n)]}{\sqrt{\sum_{i=1}^{M} 2^{-\min(i,M-1)} \sum_{n=1}^{N} s_i^2(n)/\hat{\sigma}_i^2(n)}} \,, \end{aligned} \tag{9}$$

where the time-varying channel variance estimates are given by

$$\hat{\sigma}_i^2(n) = \frac{1}{2^i K + 1} \sum_{k=n-2^{i-1}K}^{n+2^{i-1}K} x_i^2(k), i = 1, \ldots, M \,, \tag{10}$$

where each component $x_i(n)$ is periodically extended in the usual fashion and $2K + 1$ is the length of the variance estimation window for the shortest timescale.

The structure of the OWT is exceptionally convenient as it permits the efficient calculation of l for a transit pulse at any location. Note that equation (10) implies that the whitening coefficients are determined solely by $x(n)$, regardless of the assumed location of a transit signal. Thus, to compute l for a given transit pulse centered at all possible time steps, we simply "doubly whiten" $\mathbb{W}\{x(n)\}$ [i.e., divide it pointwise by $\hat{\sigma}_i^2(n)$], correlate the results with $\mathbb{W}\{s(n)\}$, and apply the dot product relation, performing the analogous operations for the denominator, noting that $\hat{\sigma}_i^{-2}(n)$ is itself a time series:

$$l(n) = \frac{\mathbb{N}(n)}{\sqrt{\mathbb{D}(n)}} = \frac{\sum_{i=1}^{M} 2^{-\min(i,M-1)} [x_i(n)/\hat{\sigma}_i^2(n)] * s_i(-n)}{\sqrt{\sum_{i=1}^{M} 2^{-\min(i,M-1)} \hat{\sigma}_i^{-2}(n) * s_i^2(-n)}} \,. \tag{11}$$

Note that the minus sign in $s_i(-n)$ indicates time reversal. The terms $\mathbb{N}(n)$ and $\mathbb{D}(n)$ are introduced for convenience later on.

Recall at this point the form of Kay's adaptive detector (eq. [4]) and the partitioning of power in each channel by the filter-bank implementation of the OWT (Fig. 4). Rather than estimating the power spectrum of the noise with a uniform moving average, equations (9) and (11) estimate $P(\omega)$ by partitioning the frequency domain into nonuniform intervals that increase in width logarithmically from the baseband. They then average the power in each channel over a time interval proportional to the inverse of the width of the channel. Clearly, an analogous operation could be carried out using periodograms rather than a wavelet transform. The efficiency of the structure of the OWT, however, provides a compelling reason not to do so. Moreover, the OWT allows one to estimate the channel variances with windows of differing lengths, an option not available with periodograms. Equation (11) forms the basis for the adaptive matched filter applied throughout the remainder of this paper. For the purposes of examining the detectability of transits against solar-like variability, however, we need only compute the expected detection statistic $\langle l \rangle$ or the S/N via

$$\langle l(n) \rangle = \sqrt{\sum_{i=1}^{M} 2^{-\min(i,M-1)} \hat{\sigma}_i^{-2}(n) * s_i^2(-n)} \,, \tag{12}$$

which holds so long as the analysis windows used to estimate $\hat{\sigma}_i^{-2}(n)$ are sufficiently long. This can be verified by examining the change in the detection statistics when $\langle x_i^2(n) \rangle$ is calculated with and without the presence of transits. Finally, we note how to combine the components of individual detection statistics to form multiple-event statistics. Suppose we wish to test for transits at widely spaced locations $A \subset \{1, \ldots, N\}$. The total detection statistic is given by

$$l_A = \sum_{i \in A} \mathbb{N}(i) \Big/ \sqrt{\sum_{i \in A} \mathbb{D}(i)} \,, \tag{13}$$

where $\mathbb{N}$ and $\mathbb{D}$ are as in equation (11). Hence, l_A can be determined from the components of the single-transit statistics at each individual transit location. The next section presents the results of our analysis of the DIARAD data set using this analysis technique.

4. RESULTS

In this section we present the results of using the DIARAD/*SOHO* data to predict the expected performance of *Kepler*, a recently selected discovery mission designed to detect Earth-sized planets orbiting solar-like stars in the cir-

cumstellar habitable zone. *Kepler* will observe more than 100,000 target stars in the Cygnus constellation continuously for at least 4 yr at a sampling rate of 4 hr^{-1} (Borucki et al. 1997). For detecting Earth-sized planets, the spectral types of the target stars span F7 through K4. The range of planetary periods of greatest interest is from a few months to 2 yr, with a corresponding range of central transit durations from $\sim$5 to 16 hr. The average transit duration is 10.1 hr for a uniform distribution of orbital periods over this range. (Note that since the average chord length[1] of a circle of unit diameter is $\pi/4$, the average duration of a transit is $\pi/4$ times the duration of a central transit, which is 13 hr at an orbital period of 1 yr. The average central transit duration over these periods happens to be $\sim$13 hr, too. Moreover, 50% of transits are longer than 11.3 hr.) The total number of effective independent tests to be performed in searching the light curves of 100,000 stars for transiting planets with orbital periods in this range is $\approx 2 \times 10^{12}$ (Jenkins et al. 2002). Assuming Gaussian statistics, a detection threshold of $\sim 7\,\sigma$ is required to control the total number of expected false alarms below 1 for the entire experiment. At this threshold, if the mean S/N of a set of transits is $\geq 8\,\sigma$, a detection rate of $\geq$84% will be achieved. As the total S/N is proportional to the square root of the number of transits, a single event S/N of $4\,\sigma$ suffices for each of a set of four transits (for a 1 yr orbit). This is a conservative requirement. It can easily be argued that the 50% detection rate achievable at a single event S/N of $3.5\,\sigma$ would yield a statistically significant sample of detections (or nondetections) given 100,000 target stars in the survey.

Kepler's aperture is 0.95 m allowing 5.75×10^9 e^- to be collected every 6.5 hr for a G2, $m_v = 12$ dwarf star for a shot noise of 13 ppm. The instrument noise should be $\sim$6 ppm over this same duration. This value is based on extensive laboratory tests, numerical studies, and modeling of the *Kepler* spacecraft and photometer (Koch et al. 2000; Jenkins et al. 2000b; Remund et al. 2001). The values in Table 3 of Koch et al. (2000) support this level of instrumental noise from a high-fidelity hardware simulation of *Kepler's* environment, while the numerical studies of Remund et al. (2001) are based on a detailed instrumental model. This model includes terms such as dark current, read noise, amplifier and electronics noise sources, quantization noise, spacecraft jitter noise, noise from the shutterless readout, and the effects of charge transfer efficiency. To simulate the combined effects of the shot noise and instrumental noise for *Kepler*, a WGN sequence was added to the DIARAD time series with a standard deviation equal to the square root of the combined shot and instrumental variance for an $m_v = 12$ star less the square of the DIARAD instrumental uncertainty (0.1 W m^{-2} in each 3 minute DIARAD measurement). The DIARAD instrumental variance is $\sim\frac{1}{4}$ the combined shot and instrumental variance for one of *Kepler's* $m_v = 12$ stars. Prior to applying the techniques of § 3, it was necessary to extend the length of the time series to a power of 2 (from $\sim 2^{17.47}$ to 2^{18} points). The time series was "periodically" extended by reflecting segments at the beginning and end of the original time series across the imaginary gap from the end to 2^{18}. Both reflected segments were tapered and added together much in the same fashion as the missing points were filled in as described in § 1. In addition, to compensate for the smoothing nature of the fill-in procedure, we computed the critically sampled WT of the extended time series and examined the local variances of the wavelet coefficients. The variances of the filled-in points were adjusted to match the variances of the points at the edges of the gaps, with a linear transition from one value to the next. This procedure was applied to each wavelet scale so long as the mean variance of the filled-in points was significantly below that of the original points. These procedures minimize edge effects attendant in performing a circular WT of a time series containing data gaps. In an actual search, care needs to be exercised near the edges of any data gaps. Any candidates with transits near data gaps should be scrutinized carefully to eliminate false positives due to edge effects.

The *Kepler* mission should not suffer from large time gaps. Roll maneuvers are planned about every 90 days to reorient the sunshade and the solar panels, as the Sun would otherwise appear to revolve about the spacecraft every year. A 24 hr period has been budgeted for thermal stability to be achieved after each roll and for nominal science operations to recommence. We assume that transits cannot be found within 12 hr prior to the roll maneuver and for 12 hr after thermal stability is achieved. The lost data amounts to $\sim$2% of the total, implying that about 2% of all transits occurring during the mission will be missed. This represents an insignificant impact on the science return as the detection of a planet does not depend on observing a set of consecutive transits. Moreover, the missing phase space can be filled in by extending the mission by about 2% or 1 month beyond the nominal 4 yr.

The OWT of the extended synthetic time series and that of a single transit were computed using Debauchies' 12 tap discrete wavelet filter (Debauchies 1988). Equation (12) was applied to transits of 6.5 hr duration and 13 hr duration with depths of 84 ppm (0.115 W m^{-2}) corresponding to an Earth-sized transit of a solar-like star. Note that we have not included limb-darkening in the simulated transits: they are simply rectangular pulses. This is a conservative approach. Limb-darkening increases the depth of nongrazing transits, providing higher total signal energy for transits with duration longer than 82% of a central transit (which holds for more than 57% of all transits). Also, limb-darkening concentrates the energy of a transit into a shorter time period. Both of these effects increase the S/N of a transit signal and increase its detectability against solar-like variability, which exhibits less power at shorter timescales. Throughout this discussion we ignore S/Ns calculated for filled-in points in the DIARAD data or from points within a day of gaps at least as long as a day. Filled-in points do influence the results of nearby non–filled-in points since they are included in the calculation of local variance estimates of other points (see eq. [10]). Their influence is reduced by the compensation scheme described earlier. Figure 5 shows the results as a function of time throughout the 5.2 yr DIARAD data record. Note that the S/N of a 13 hr transit is significantly higher than that of a 6.5 hr transit at the beginning of

[1] Here we must be clear about how "random" chords are generated. For circular orbits, the sole parameter determining whether a planet transits or not is orbital inclination, i. Assuming that i is uniformly distributed implies that the distance of chords from the center of the stellar disk for transiting planets, a, is also uniformly distributed. The average chord length, $\bar{c}$, of chords constructed in this manner for a unit-diameter disk is then $\int_0^{1/2} 2(1/4 - a^2)^{1/2} da / \int_0^{1/2} da$ or $\pi/4$, giving the ratio of $\bar{c}$ to the maximum chord length, 1, as $\pi/4$.

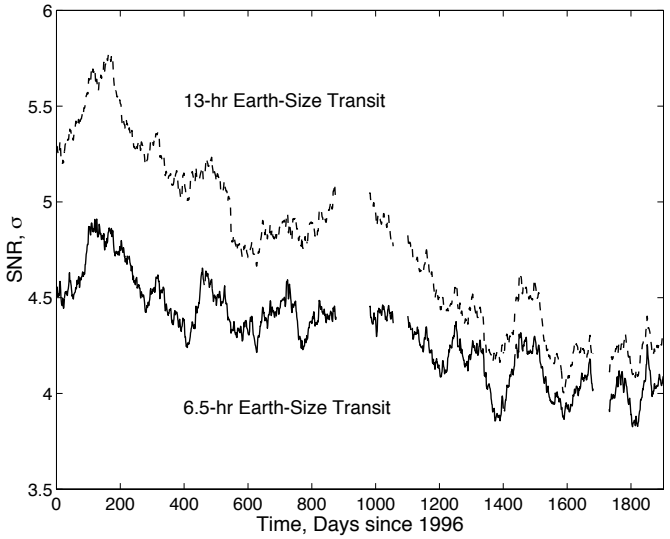

FIG. 5.—Estimated S/Ns (in σ) for 6.5 and 13 hr transits of Earth-sized planets orbiting $m_v = 12$ Sun-like stars over half a solar-like cycle. Values of S/N greater than 4 σ indicate a detection rate exceeding 84% for four transits.

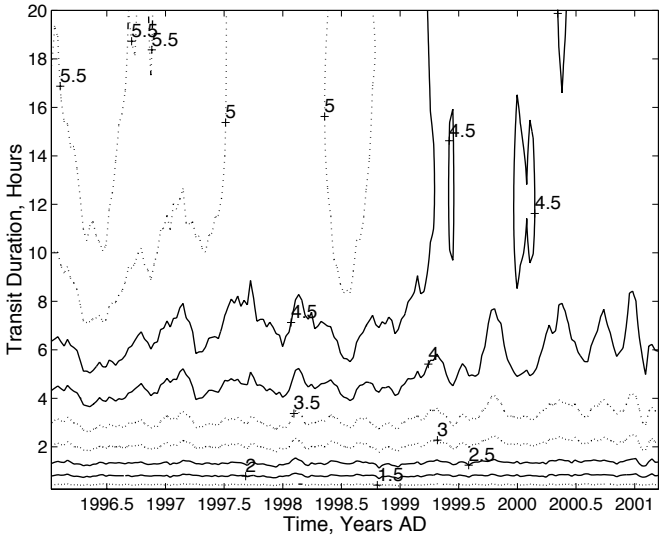

FIG. 7.—Contour map of estimated S/Ns (in σ) for single transits of Earth-sized planets orbiting $m_v = 12$ Sun-like stars with durations from 0.25 to 20 hr. Four or more Earth-sized transits longer than ~5 hr are detectable ≥84% of the time.

the data record near solar minimum (~5.7 vs. ~4.9 σ) but that it is nearly the same at the end of the record near solar maximum (~4.25 vs. ~4 σ). This is a consequence of the movement of noise power toward shorter timescales as solar maximum is approached (see Fig. 2). Another way to interpret the S/Ns plotted in this figure is to examine the equivalent total noise in a time interval equal to the duration of the transit. This is easily computed by dividing the transit depth (84 ppm) by the S/N. Figure 6 shows the result of this calculation for the 6.5 and 13 hr transits. As the desired total noise for *Kepler* is to have no more than 21 ppm for the total noise budget at 6.5 hr (for an $m_v = 12$ star), it is clear that this requirement is met with significant margin over most of the data record. Since transit photometry campaigns search for sequences of transits, it is the mean S/N that is of interest, not the S/N of any particular transit. These calculations were extended to cover transits of durations of 0.25–20 hr. Figures 7 and 8 present contour maps of the S/N and equivalent total noise over the course of the DIARAD observations with instrumental and shot noise expected for *Kepler*. The S/Ns allow *Kepler* to detect Earth-sized planets exhibiting four transits longer than ~5 hr for $m_v = 12$ stars.

We note that minimum detectable planet radius is not particularly sensitive to the single-event S/N as this is proportional to the square of the planetary radius. To illustrate this, we extend the calculations above to stars of magnitude other than $m_v = 12$. The uncertainty of the DIARAD time series is equivalent to the combined shot and instrumental

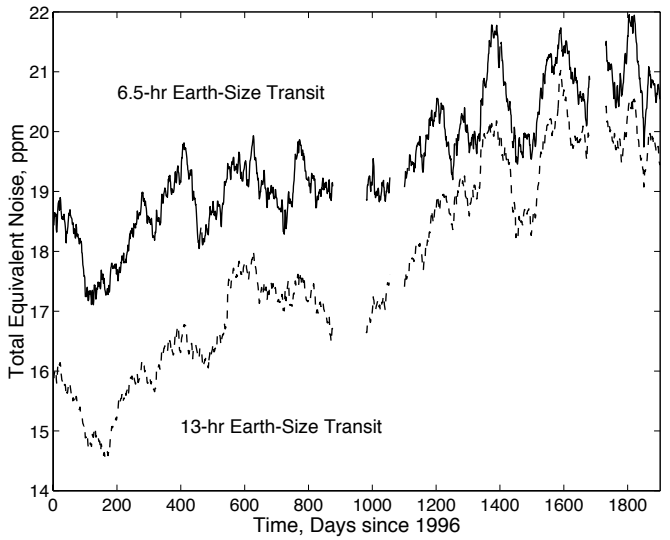

FIG. 6.—Equivalent total noise (in ppm) for 6.5 and 13 hr transits of Earth-sized planets orbiting $m_v = 12$ Sun-like stars over half a solar-like cycle. *Kepler's* total noise budget is set to no more than 21 ppm at a timescale of 6.5 hr, including stellar variability (i.e., 4 σ for an 84 ppm Earth-sized transit). This requirement is met with significant margin on average for the noise environment expected for *Kepler*.

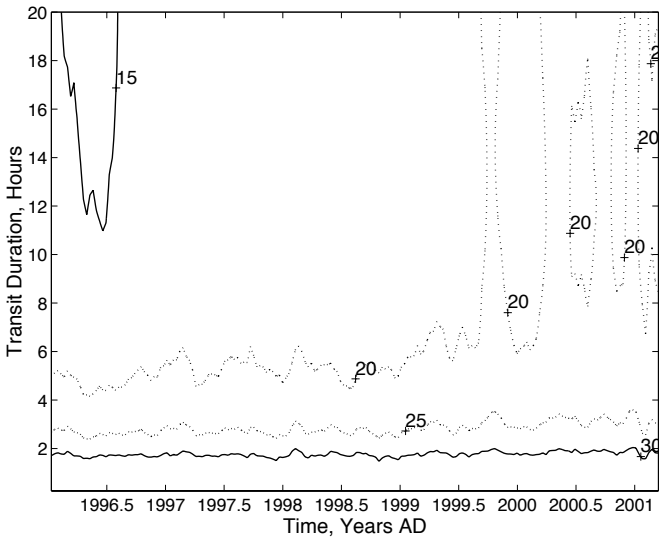

FIG. 8.—Contour map of the equivalent total noise (in ppm) as a function of transit duration (or time interval) for Earth-sized transits with shot and instrumental noise appropriate for the *Kepler* mission.

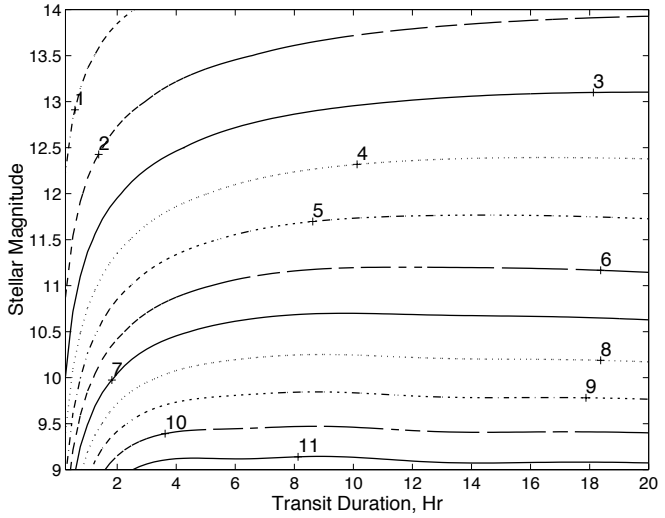

FIG. 9.—Contour map of the Earth-sized, single-transit S/N (in σ) as a function of stellar magnitude and transit duration. The range of stellar magnitudes corresponds to the range for *Kepler's* target stars.

noise of a $m_v = 10.4$ star. To simulate data from stars brighter than this required "denoising" the DIARAD time series to remove the instrumental noise. To do this, we multiplied each channel of the decimated WT of the 15 minute binned DIARAD time series by a scalar equal to the square root of the ratio of the sample variance less the DIARAD instrumental variance to the sample variance and then transformed the result back into the time domain. This operation is essentially a Wiener filter implemented in the wavelet domain. Noise sequences representing a combination of shot noise and *Kepler* instrumental noise were then added to the "denoised" time series to simulate data from stars of different magnitudes. The sample variances of the first few channels are actually slightly less than the reported measurement uncertainties. We believe that this is likely the result of the measurement-replacement procedure we used. Alternatively, it may be due in part to an overly conservative estimate of the instrument sensitivity by the DIARAD science team. In any case, the difference between the reported variance and the actual sample variance is small. At the point design for a $m_v = 12$ star, the difference is relatively insignificant since the shot noise for such a star is well above the reported DIARAD measurement uncertainty. For the first several channels (short timescales), then, we simply set the scalar to zero when the operation given above yielded an imaginary number. This is in one respect a conservative approach as it places more noise in these channels than in the original time series for a given magnitude star.

Figure 9 shows a contour map of the Earth-sized, single-transit S/N as a function of stellar magnitude and transit duration. We obtain S/Ns as high as 11 σ for $m_v = 9$ stars, while S/Ns as low as 1 σ are obtained at $m_v = 14$ for transits longer than 2.5 hr. Values for the minimum detectable planetary radius at an 84% detection rate for four and for six transits are given in the contour maps of Figure 10. This figure demonstrate that planets significantly smaller than Earth can be found by *Kepler*. For example, at $m_v = 10$ and for four transits, planets with radii as small as 0.7 $R_\oplus$ are detectable (0.5 Earth areas). With six transits, planets with radii as small as 0.6 $R_\oplus$ (0.36 Earth areas) are detectable. Additionally, for cases exhibiting six transits, planets as small as 1.0 $R_\oplus$ can be detected orbiting stars as dim as $m_v = 12.7$. Keep in mind that this is for a detection rate of 84%. Planets smaller than these are still detectable at lower detection rates.

Finally, we use the DIARAD time series to estimate the effect of stellar rotation period on the detectability of terrestrial planets. Batalha et al. (2002) estimate that 65% of *Kepler's* target stars (F7–K9) are sufficiently old to have spun down to rotation periods $\geq$20 days. The question is how is the detectability of transits affected by rotation periods experienced by the majority of these target stars? Ground-based observations show that solar-type stars rotating faster than the Sun are more magnetically active, increasing the photometric variability over a range of timescales. These observations provide an indication of the appropriate scaling relation to use on timescales greater than 1 day. Figure 7

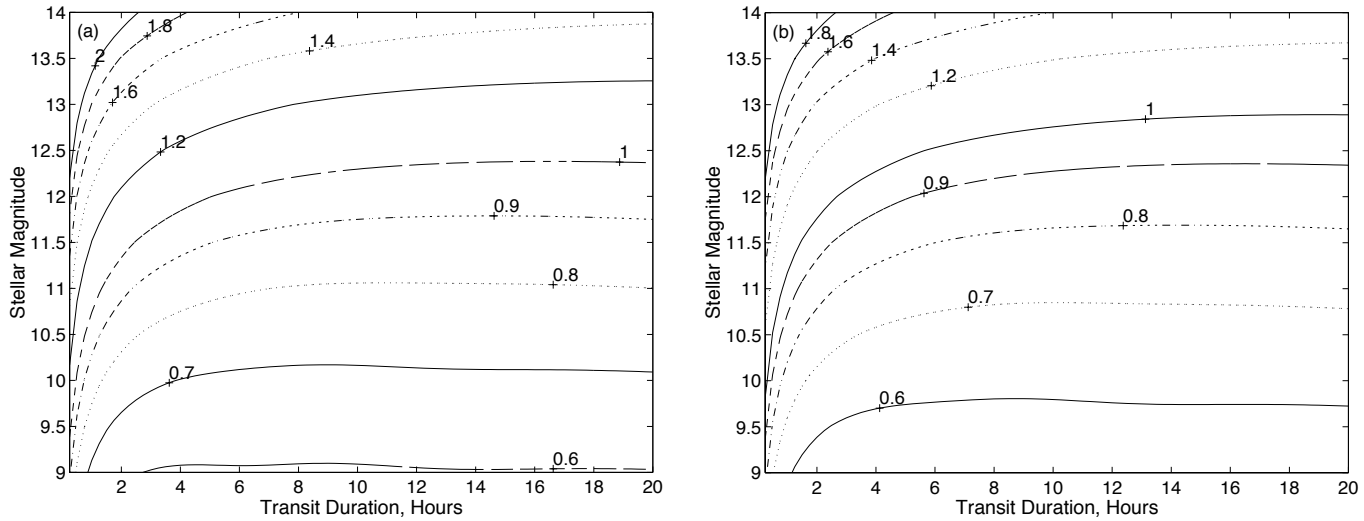

FIG. 10.—Contour map of the minimum detectable planetary radius ($R_\oplus = 1$) at the 84% detection rate as a function of stellar magnitude and transit duration for planets exhibiting (*a*) four transits and (*b*) six transits. At $m_v = 10$ and for four transits, planets with radii as small as 0.7 $R_\oplus$ are detectable (0.5 Earth areas). With six transits, planets with radii smaller than 0.6 $R_\oplus$ (0.36 Earth areas) are detectable.

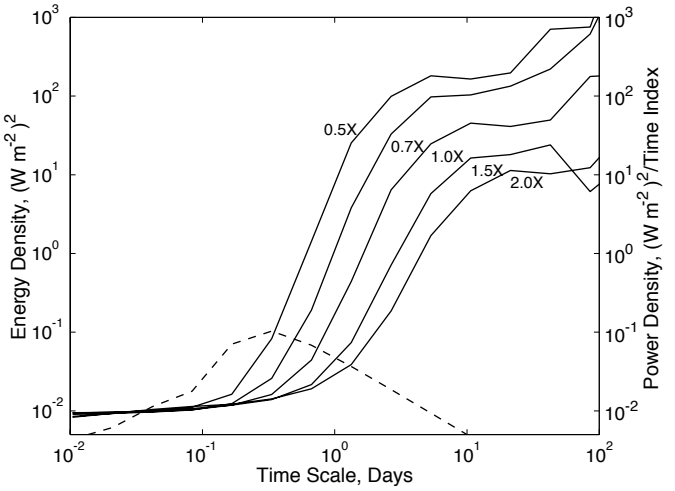

FIG. 11.—Distribution of power as a function of timescale from wavelet analyses of simulated time series of solar-like stars rotating both faster and slower than the Sun. The labeled solid lines are for stars with rotation periods between 0.5 $P_\odot$ and 2.0 $P_\odot$ ($P_\odot = 26.6$ days), while the dashed curve shows the energy density of a 10 hr, Earth-sized transit. As the rotation period decreases, the power spectrum shifts left toward shorter timescales, and upward as well, due to increased photometric variability, and hence, "swallows" more transit energy. Earth-sized transits remain detectable for stars rotating as much as twice as fast as the Sun, so long as a sufficient number of transits ($\sim$7) are observed.

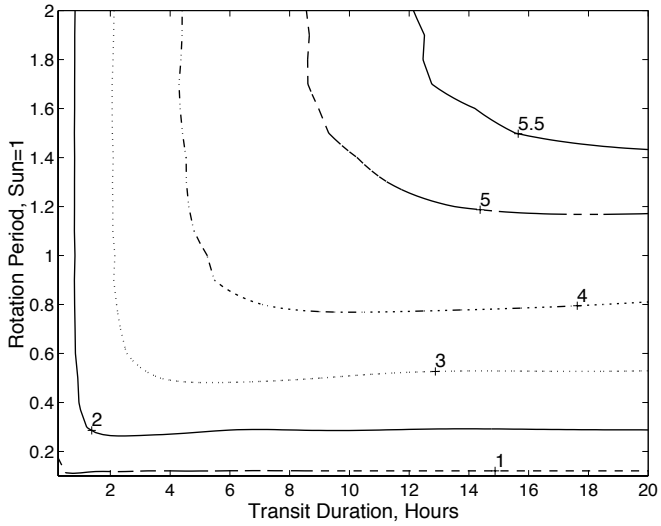

FIG. 12.—Contour map of the mean Earth-sized, single-transit S/N (in σ) as a function of transit duration and stellar rotation period for $m_v = 12$, G2 stars in *Kepler's* FOV. Mean S/Ns exceeding 4 σ indicate a detection rate of at least 84% for four or more transits.

of Radick et al. (1998) indicates that photometric variability, $\sigma_{\rm phot}$, on timescales shorter than a year is related to the chromospheric activity level parameter, $R'_{\rm HK}$, by a power law with exponent 1.5. Other observations (Noyes et al. 1984) suggest that $R'_{\rm HK}$ is approximately inversely proportional to stellar rotation period, $P_{\rm rot}$, so that

$$\sigma_{\rm phot} \approx P_{\rm rot}^{-1.5} \ . \qquad (14)$$

What these ground-based studies do not provide, however, is the relation between rotation period and photometric variability on timescales shortward of a few days. The DIARAD measurements represent a means by which the timescale-dependent response of solar-like stars to increased magnetic activity can be estimated. At solar maximum (with high magnetic activity levels), variability at long timescales increases significantly relative to solar minimum, while it remains comparatively constant at timescales of hours (see Fig. 2). To generate a synthetic time series for an arbitrary rotation period, then, we first scale the variances of the OWT of the filled-in DIARAD time series (binned to 15 minutes) according to equation (14) and the ratio of the curves in Figure 2, so that the scaling ramps from a factor of 1 at the shortest timescale up to the value given by equation (14) by the ninth timescale ($\approx$2.66 days). Next, the inverse OWT is performed, and the resulting time series is resampled by linear interpolation onto the appropriate time grid. Finally, *Kepler's* combined shot and instrumental noise for $m_v = 12$ stars is added to the resampled time series. This procedure represents our best estimate of how stellar rotation period should affect the photometric variability of solar-like stars. We do not expect this model to be accurate over a wide range of stellar types. It probably is indicative only of the expected effects over stellar types near the Sun (G1–G4). Earlier type stars generally exhibit less spotting and consequently, lower $\sigma_{\rm phot}$, while later type stars exhibit more spotting and higher $\sigma_{\rm phot}$ for a given $P_{\rm rot}$ (see, e.g., Messina, Rodono, & Guinan 2001). Earlier type stars, however, are larger, requiring a larger planet to achieve the same S/N for a given photometric variability, while later type stars are smaller, mitigating the increased variability for a given size planet to some degree. This analysis does not include the effects of flare events, which exhibit transient signatures on timescales of minutes (more frequently) to a few hours (more rarely), the frequency of which increases significantly for rapid rotators.

Keeping these limitations in mind, we investigated rotation periods from as short as one-tenth to as long as twice that of the Sun, where we adopt a mean projected solar rotation period, $P_\odot$, of 26.6 days. Figure 11 shows the power density as a function of timescale for $m_v = 12$, solar-like stars with $0.5\ P_\odot \leq P_{\rm rot} \leq 2.0\ P_\odot$, along with the energy density of a 10 hr, Earth-sized transit. As $P_{\rm rot}$ decreases, more transit energy is masked, decreasing the detectability. On the other hand, as $P_{\rm rot}$ increases, more transit energy leaks through the background noise, aiding in detection. Figure 12 shows the mean S/N determined over rotation periods between 0.1 $P_\odot$ and 2.0 $P_\odot$ and as a function of transit duration from 0.25 to 20 hr. The single-transit S/N exceeds 4 σ for transits longer than 7 hr and $P_{\rm rot} \gtrsim 21$ days, giving a detection rate $\geq$ 84% for four or more such transits. (We note that applying the scaling relation of eq. [14] to all timescales uniformly results in a value of 3.5 σ for similar duration transits and rotation periods, yielding a 50% detection rate.) Figure 13 shows contour plots of the minimum detectable planet radius at the 84% detection rate for four transits (Fig. 13*a*) and for six transits (Fig. 13*b*) as functions of transit duration and stellar rotation period. Six 3 hr or longer transits are sufficient to detect an Earth-sized planet for $P_{\rm rot} \gtrsim 16$ days. *Kepler* stands a good chance of detecting planets at least as small as Earth orbiting stars with rotation periods 40% shorter than that of the Sun.

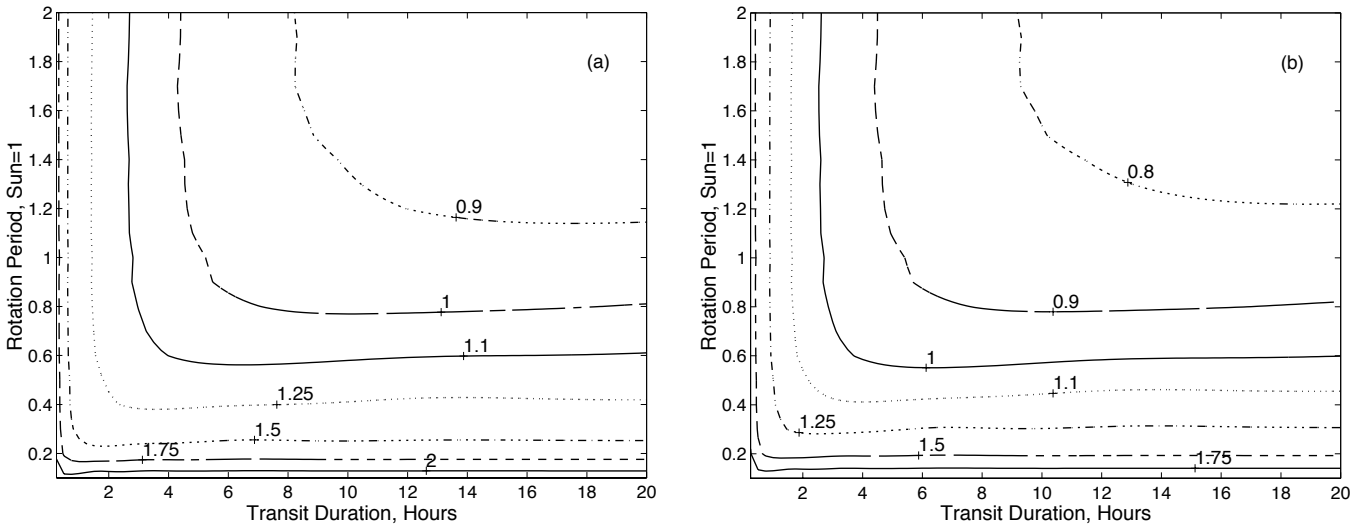

FIG. 13.—Contour maps of the minimum detectable planetary radius ($R_\oplus = 1$) at the 84% detection rate as a function of transit duration and stellar rotation period for planets exhibiting (*a*) four transits and (*b*) six transits. Instrument and shot noise appropriate for $m_v = 12$, G2 stars in *Kepler's* FOV is included in the analysis. Transiting Earth-sized planets exhibiting six transits are detectable around stars with rotation periods 40% shorter than that of the Sun ($P_{\rm rot} \approx 16$ days).

5. ASSESSING THE NORMALITY OF THE DIARAD DATA

The interpretation of the S/Ns obtained in § 4 in terms of detection probability depend on the distribution of the null statistics. If the observation noise is significantly non-Gaussian, equation (3) may underestimate the false-alarm rate for a given threshold, and so the detection rate may be lower than that indicated by equation (2) once a reasonable threshold is determined. In this section we characterize the distribution of null statistics for simulated *Kepler* data. We then assess its similarity to a Gaussian distribution in terms of the threshold required for a given false-alarm rate. We note first that even if the distribution of the individual null statistics is significantly non-Gaussian, the distribution of the null statistics for multiple transits may be approximately Gaussian. This is due to the tendency of linear combinations of random variables to approach a Gaussian distribution (Papoulis 1984). To address this question, we apply a bootstrap approach similar to that described in Jenkins et al. (2002). The modified algorithm is described in the Appendix.

One might wonder whether solar-like variability produces transit-like features that might be confused with actual transit events. It is a curious characteristic of random processes that they can, indeed, produce any given feature if observed for a sufficient length of time. The DIARAD data set is no exception. There are several transit-like features over the 5.2 yr data set. The S/N of these features is no more than 5 σ, and only a handful exhibit detection statistics larger than 4 σ. The number of such events is somewhat higher than one would expect from Gaussian noise. The average Earth-sized transit yields a detection statistic of $\sim$8 σ against this noise. Thus, even though there are some transit-like features, they are individually much less significant than an Earth-sized transit event would be. The question to answer is this: how great is the likelihood that a number of such features would occur with a purely periodic separation, so that the total S/N exceeds the detection threshold? To answer this question, we examine the bootstrap distribution of the null statistics of searches for sets of four 8 hr transits in the DIARAD data set.

Figure 14 shows the false-alarm rate as a function of detection threshold for the bootstrap statistics for the bare DIARAD data, along with those for simulated *Kepler* data for an $m_v = 12$ star, and for that expected for Gaussian noise. The range of false-alarm rates extends from 10^{-10} to 10^{-15}. At the required false-alarm rate of 10^{-12} for *Kepler*, the curves indicate thresholds of 7.04, 7.18, and 7.52 σ, respectively, for Gaussian noise, for noise appropriate for a

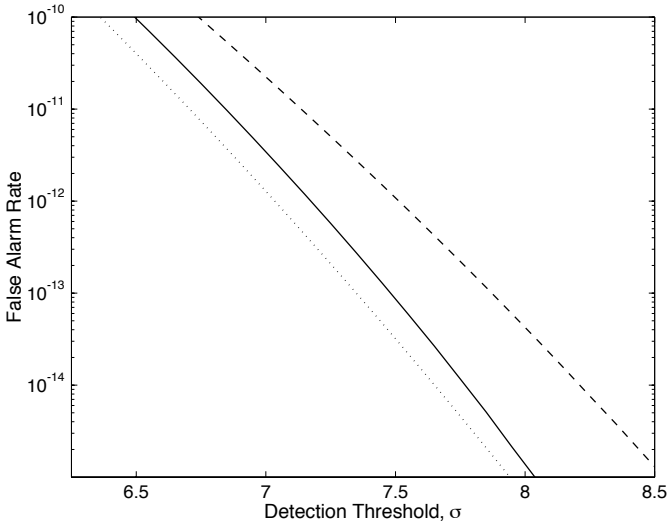

FIG. 14.—Graph of the false-alarm rate as a function of detection threshold for a search for four 8 hr transits in the DIARAD data. The dotted line is for Gaussian noise, the solid line is for the DIARAD data plus shot and instrumental noise appropriate for an $m_v = 12$ star, and the dashed curve is for the DIARAD data with no additional noise. Although the null statistics of the DIARAD data are significantly non-Gaussian, the combination of statistics for searches for four or more transits results in a distribution that is fairly well characterized as Gaussian. When the additional shot and instrumental noise for an $m_v = 12$ star is included, the resulting distribution is nearly Gaussian.

$m_v = 12$ *Kepler* star, and for DIARAD data with no instrumental or shot noise added. Thus, to reach a false-alarm rate appropriate for *Kepler*, we would need to increase the detection threshold above that for Gaussian noise by only 0.14 σ for a $m_v = 12$ star, and by $\sim$0.5 σ for very bright stars ($m_v \leq 10.4$). This reduces the detection rate to 80% at $m_v = 12$. At $m_v \leq 12$, however, the detection rate is reduced by an insignificant amount as the S/N for four Earth-sized transits is $\sim$16 σ at these stellar magnitudes, which is much higher than the revised detection threshold of 7.5 σ. Therefore, even though solar-like stars may exhibit occasional transit-like features (as would any random process), the frequency and strength of such features does not significantly increase the detection threshold that is required to limit the total number of false alarms over the entire campaign to no more than one. Thus, natural solar-like variations pose no threat to the ability of transit photometry to detect planets as small as Earth, assuming that a sufficient number of transits is observed.

6. CONCLUSIONS

Determining the frequency of Earth-sized planets orbiting solar-like stars in the Sun's galactic neighborhood is a high priority for both NASA and ESA. Several missions have been proposed with the capability to detect such planets, including NASA's *Kepler* mission and ESA's *Eddington* mission. The ability of such missions to achieve their awe-inspiring goals is limited by the intrinsic variability of solar-like stars. Currently, the only solar-like star for which data exist with the high temporal sampling and low measurement noise required to address this topic is the Sun. Measurements made by the DIARAD instrument on board *SOHO* considered here nearly contiguously sample the Sun's irradiance over nearly half a solar cycle (5.2 yr). We analyzed this data set using a wavelet-based technique that yields a realizable and near-optimum detector that is efficient and flexible. Future work will seek to improve the adaptive wavelet detector by seeking wavelet pairs optimally chosen for the detection of transit signatures. For example, Chapa & Rao (2000) provide a method for designing mother wavelets matched to a given signal. For the overcomplete wavelet transform, some of the constraints on the wavelets allowing them to be used in critically sampled applications may be relaxed, resulting in filters with shorter transition bands and/or better isolation of transit signatures at a single timescale. In addition, more physically realistic models for stellar variability of solar-like stars rotating at arbitrary periods should be pursued and then analyzed using the methodology presented here. A bootstrap analysis of the null statistics for the DIARAD data indicates that the observational noise for *Kepler* yields approximately Gaussian detection statistics. Thus, the required detection threshold and expected detection probabilities can be reliably estimated, assuming Gaussian statistics. The results of the analysis indicate that broadband, white-light photometric variability of solar-like stars is not an impediment to the detection of transiting planets, as most of the variability occurs on timescales comparable to and longer than the stellar rotation period, which is much longer than a typical transit. Indeed, *Kepler* and *Eddington* are likely capable of detecting Earth-sized planets orbiting solar-like stars rotating significantly faster than the Sun.

I thank Natalie Batalha (NRC Postdoctoral Fellow), Laurance Doyle (SETI Institute), William Borucki (NASA Ames Research Center), Douglas Caldwell (SETI Institute), and Ron Gilliland (STScI) for their careful reading of the manuscript and their suggestions for improvement. I thank Renée Schell for her careful proofreading of the manuscript and editorial suggestions and David Koch (NASA ARC) for help with graphics. I appreciate the careful work of Steve Saar (Harvard-Smithsonian CfA), who reviewed the manuscript, for his suggestions for improvement, especially as regards the issue of stellar rotation. I acknowledge the efforts of the VIRGO team. VIRGO is an investigation on the solar and heliospheric observatory *SOHO*, which is a mission of international cooperation between ESA and NASA. This work was supported by funding from Origins and Advanced Project Offices at NASA Headquarters and the Astrobiology Office at NASA Ames Research Center.

APPENDIX

A MODIFIED BOOTSTRAP ALGORITHM FOR DETERMINING THE DISTRIBUTION OF THE NULL STATISTICS FOR A TRANSIT SEARCH

Here we outline the computational algorithm used to explore the bootstrap statistics of a search for several transits, given a time series representing observational noise. This is a necessary step in determining an appropriate detection threshold for a photometric transit campaign. The goal is to determine what the distribution of the null statistics is for multiple transits from a knowledge of null statistics corresponding to single-transit events. A direct examination of the multiple-event statistics for a data set such as from DIARAD is numerically prohibitive. Jenkins et al. (2002) provide a Monte Carlo approach for examining such distributions, which can be computationally quite intensive. The approach given here allows one to concentrate efficiently on the upper tail of the distribution, which is often of greatest interest. First, assume that the single-event statistics have been computed and that they have been sorted in descending order. Further assume that the numerator and denominator from equation (9) have been preserved, so that multiple-event statistics can be computed from the components of the single-event statistics. Now the bootstrap statistics for a search for L transits consist of forming the multiple-transit statistics for all possible combinations of L events. For the DIARAD data set, there are $\sim$150,000 time steps, for a total of over 4×10^{20} possible combinations for four transits. Clearly, forming the sample distribution for such a large number of points is out of the question. We can, however, sort the single-event statistics and sample the distribution of interest in a practical manner, obtaining a histogram at any desired resolution.

Note that there is no natural a priori ordering for multiple-event statistics in terms of the component single-event statistics owing to the manner in which the former are formed from the latter. However, the higher multiple-event statistics will tend to

be produced by combinations of high single events. Thus, it is possible to examine the bootstrap distribution of the multiple-event statistics roughly from highest to lowest over a given range of values. We give the example for four transits, but the algorithm can be easily generalized to any number of transits. Begin with a counter set at [1, 1, 1, 1]. This indicates the combination of four transits each identical to the event with the largest single-event statistic. Here we assume a lower threshold of 6 σ for the range of statistics of interest and a given bin size ($\ll$1). The multiple-event statistic corresponding to this combination of the ordered single-event statistics is formed, and the histogram bin containing this statistic is incremented by 1 (the number of ways to draw this combination of statistics at random). The counter is incremented by one to [1, 1, 1, 2], the corresponding statistic is formed and the corresponding histogram bin incremented by 4, the number of permutations of this set of digits. This procedure is continued until a statistic is encountered that is below the lower threshold (of 6 σ for this example). At this point, the second digit (from the right) of the counter is incremented to 2, the first is set to 2: [1, 1, 2, 2], and the procedure is continued. At any point that a statistic is encountered below 6 σ, the next higher digit from the one that was previously incremented is itself incremented. This criterion prevents the algorithm from needlessly considering multiple-event statistics below the range of interest ($<$6 σ here). Additionally, the monotonicity of the counter digits is preserved with every increment. In this way, assuming no lower threshold for skipping combinations, all possible combinations would be considered. At the termination of the algorithm, the number of events in each bin are divided by the total possible number of combinations of events to form a histogram of the probability density distribution above 6 σ. Note that the resulting histogram will not be accurate in the neighborhood of the lower threshold, as many statistics that somewhat exceed this bound are not considered because of the lack of a natural a priori ordering for the multiple-event statistics. Hence, the lower threshold should be set conservatively below the actual range of interest. For the DIARAD data, reliable results are obtained above $\sim$6.25 σ. The false-alarm rate as a function of threshold is obtained by taking 1 minus the cumulative sum of the density histogram and noting that the threshold is the left edge of each histogram bin.

This procedure may still be too taxing in computational terms. For example, assume that the lower threshold is 6 σ and that there are 146,000 single events. Gaussian statistics imply that events greater than this threshold occur with frequency 10×10^{-10}. So we would expect the procedure above to terminate after approximately 4.5×10^{11} iterations. In this case, the procedure can be sped up by sampling, either deterministically or randomly. For deterministic sampling, instead of incrementing the counter by 1, it can be incremented by a fixed value greater than 1, say 100. Alternatively, the counter can be incremented by a discrete positive random deviate with a mean of 25, for example. Such deviates can be obtained simply by taking the nearest integer larger than the product of a uniform random deviate in the interval [0, 1] and twice the desired mean increment. The resulting histogram must be multiplied by the mean increment value to account for the missing values. For the examples discussed in § 5, the counter was randomly incremented with a mean increment of 25 and a histogram bin size of 0.1 σ.

REFERENCES

Batalha, N., M., Jenkins, J., Basri, G. S., Borucki, W. J., & Koch, D. G. 2002, in Proc. 1st Eddington Workshop, Stellar Structure and Habitable Planet Finding, ed. B. Battrick (Noordwijk: ESA), 35
Bordé, P., Rouan, D., & Léger, A. 2001, CR Acad. Sci. Paris, 2, 1049
Borucki, W. J., Caldwell, D. A., Koch, D. G., Webster, L. D., Jenkins, J. M., Ninkov, Z., & Showen, R. L. 2001, PASP, 113, 439
Borucki, W. J., Koch, D. G., Dunham, E. W., & Jenkins, J. M. 1997, in ASP Conf. Ser. 119, Planets Beyond the Solar System and The Next Generation of Space Missions, ed. D. Soderblom (San Francisco: ASP), 153
Borucki, W. J., Scargle, J. D., & Hudson, H. S. 1985, ApJ, 291, 852
Borucki, W. J., & Summers, A. L. 1984, Icarus, 58, 121
Brown, T. M., & Charbonneau, D. 2000, in ASP Conf. Ser. 219, Disks, Planetesimals, and Planets, ed. F. Garzón & T. J. Mahoney (San Francisco: ASP), 54
Brown, T. M., Charbonneau, D., Gilliland, R. L., Noyes, R. W., & Burroughs, A. 2001, ApJ, 552, 699
Castellano, T., Jenkins, J. M., Trilling, D. E., Doyle, L. R., & Koch, D. G. 2000, ApJ, 532, L51
Chapa, J. O., & Rao, R. M. 2000, IEEE Trans. Sig. Proc., 48, 3395
Charbonneau, D., Brown, T. M., Latham, D. W., & Mayor, M. 2000, ApJ, 529, L45
Debauchies, I. 1988, Commun. Pure Appl. Math., 41, 909
Deeg, H. J., et al. 1998, A&A, 338, 479
Deeg, H. J., Favata, F., & the *Eddington* Science Team 2000, in ASP Conf. Ser. 219, Disks, Planetesimals, and Planets, ed. F. Garzón & T. J. Mahoney (San Francisco: ASP), 578
Defay, C., Deleuil, M., & Barge, P. 2001, A&A, 365, 330
Doyle, L. R., et al. 2000, ApJ, 535, 338
Dravins, D., Lindegren, L., Mezey, E., & Young, A. T. 1998, PASP, 110, 610
Everett, M. E., Howell, S. B., van Belle, G., & Ciardi, D. 2002, PASP, 114, 656
Frandsen, S., Dreyer, P., & Kjeldsen, H. 1989, A&A, 215, 287
Fröhlich, C., et al. 1997, Sol. Phys., 175, 267
Gilliland, R. L., & Brown, T. 1992, PASP, 104, 582
Gilliland, R. L., et al. 2000, ApJ, 545, L47
Henry, G. W. 1999, PASP, 111, 845
Henry, G. W., Marcy, G. W., Butler, R. P., & Vogt, S. S. 2000, ApJ, 529, L41
Jenkins, J. M., Borucki, W. J., Dunham, E. W., & McDonald, J. S. 1997, in ASP Conf. Ser. 119 Asymmetrical Planetary Nebulae II, ed. D. Soderblom (San Francisco: ASP), 277
Jenkins, J. M., Caldwell, D. A., & Borucki, W. J. 2002, ApJ, 564, 495
Jenkins, J. M., Doyle, L. R., & Deeg, H. J. 2000, Acta Astron., 46, 693
Jenkins, J. M., Witteborn, F., Koch, D. G., Dunham, E. W., Borucki, W. J., Updike, T. F., Skinner, M. A., & Jordan, S. P. 2000, Proc. SPIE, 4013, 520
Kay, S. 1999, IEEE Trans. Sig. Proc., 47, 10
Koch, D. G., Borucki, W. J., Dunham, E. W., Jenkins, J. M., Webster, L., & Witteborn, F. 2000, Proc. SPIE, 4013, 508
Laughlin, G. 2000, ApJ, 545, 1064
Messina, S., Rodono, M., & Guinan, E. F. 2001, A&A, 366, 215
Noyes, R. W., Hartmann, L., Baliunas, S. L., Dunkan, D. K., & Vaughan, A. H. 1984, ApJ, 279, 763
Olsen, E. H. 1977, A&A, 58, 217
Papoulis, A. 1984, Probability, Random Variables, and Stochastic Processes (New York: McGraw Hill)
Radick, R. R., Lockwood, G. W., Skiff, B. A., & Baliunas, S. L. 1998, ApJS, 118, 239
Remund, Q. P., Jordan, S. P., Updike, T. F., Jenkins, J. M., & Borucki, W. J. 2001, Proc. SPIE, 4495, 182
Riedel, K. S., & Sidorenko, A. 1995, IEEE Trans. Sig. Proc., 43, 188
Robichon, N., & Arenou, F. 2000, A&A, 355, 295
Robinson, L. B., Wei, M. Z., Borucki, W. J., Dunham, E. W., Ford, C. H., & Granados, A. F. 1995, PASP, 107, 1094
Schneider, J., & Chevereton, M. 1990, A&A, 232, 251
Smith, M. J. T., & Barnwell, T. P., III. 1984, inProc. IEEE Int. Conf. Acoust., Speech, and Sig. Proc., San Diego, CA
Vetterli, M., & Kovačević, J. 1995, Wavelets and Subband Coding (Englewood Cliffs: Prentice-Hall)
Walden, A. T., Percival, D. B., & McCoy, E. J. 1998, IEEE Trans. Sig. Proc. 12, 3153
Young, A. T., et al. 1991, PASP, 103, 221